

Article

# Analysis of Failure Mode of Reinforced Embankments Overlying Voids Based on Discrete Method

Qi Zhang and Yongliang Lin \*

School of Mechanics and Engineering Science, Shanghai University, Shanghai 200444, China;  
zq86184265@shu.edu.cn

\* Correspondence: lin\_yliang@163.com

**Abstract:** The mode of the reinforced embankment overlying voids was generated based on discrete element software. By changing the vertical distance  $H$  and the horizontal distance  $L$ , the influence of the void position on the bearing capacity characteristics, displacement field, stress field and its reinforcement deformation law of the reinforced embankment was analyzed when a local overload was applied. Numerical simulation results show that the vertical displacement of the geogrid is symmetrical around the center of the loading plate, and the transverse displacement of the geogrid shows a centrosymmetric trend around the center of the loading plate at different void locations. In addition, the failure mode of the embankment at different void positions is proposed. Four different failure modes exist for the reinforced embankments overlying voids under local overloading: perforation failure, collapse perforation failure, void side failure and no impact failure. When  $L = 0$ , as  $H$  increases, the embankment failure mode changes from perforation failure to collapse perforation failure; and when  $L > 0$ , as  $L$  increases, the failure mode changes from void side failure to no impact failure.

**Keywords:** failure modes; reinforced embankments; voids; discrete elements



**Citation:** Zhang, Q.; Lin, Y. Analysis of Failure Mode of Reinforced Embankments Overlying Voids Based on Discrete Method. *Appl. Sci.* **2023**, *13*, 9270. <https://doi.org/10.3390/app13169270>

Academic Editors: Raffaele Zinno and José Manuel Moreno-Maroto

Received: 10 July 2023

Revised: 12 August 2023

Accepted: 14 August 2023

Published: 15 August 2023



**Copyright:** © 2023 by the authors. Licensee MDPI, Basel, Switzerland. This article is an open access article distributed under the terms and conditions of the Creative Commons Attribution (CC BY) license (<https://creativecommons.org/licenses/by/4.0/>).

## 1. Introduction

With the gradual laying of the traffic road network in recent years, the environment of road construction has become more and more complex. Some voids are difficult to detect during the survey process and are gradually enlarged by the self-weight of the embankment or the traffic load during road operation, thus causing road collapse accidents [1–4]. Currently, the horizontal reinforcement method is widely used in engineering to prevent the sudden settlement and instability of embankments caused by overlying voids [5,6]. Based on the demand of engineering applications, many experts have performed a lot of research in the field of horizontal reinforcement method to prevent voids. The reasonableness of geosynthetic materials to prevent voids was verified via tests [7,8]. Kinney [9] analyzed the deformation characteristics of reinforced bodies. The results demonstrated that a geosynthetic material deflection curve did not completely fit a circular nor a parabolic shape. Huang [10] revealed that the friction angle and particle size within the soil had obvious influence on the deformation and tension of the reinforcement material with the help of a trapdoor test model. Lu [11] analyzed the stress–strain characteristics of the reinforced body and found that the peak tensile strain in the bottom layer of the geogrid was at the edge of the void. Huckert [12] analyzed the effect of void span on soil displacement and reinforced body deformation during traffic loading. Chevalier [13] analyzed the load transfer mechanism and the slip surface shape of the upper part of the void. Benmebarek [14] used PLAXIS to study the effect of reinforcement length and stiffness on the settlement of reinforced embankments overlying voids. By means of finite element combined with discrete element methods, the mechanism of force transfer between the soil and reinforcement was investigated and revealed from a microscopic viewpoint [15,16].

Li [17] compared and analyzed the deformation of the reinforced body under three types of load distribution, and concluded that it was economical and reasonable to use the inverted triangular distribution. Feng [18] considered the vertical deformation of the soil in the anchorage area and proposed a method for calculating the deformation of the reinforced body. Chen [19] considered the effect of soil cohesion in the design of the calculation method. A more systematic study of reinforced embankments where the void has collapsed below the reinforced body has been presented in the above literature.

In practical engineering, a portion of soil may exist between the void and the reinforcement material in the embankment. For such conditions, Das [20] investigated the relationship between void depth and embankment bearing capacity. Wu [21] studied the effect of eccentric load and load eccentricity on the bearing capacity characteristics of the void embankment. Zhou [22] took a square void embankment as the object of study to investigate the effect of the property of the fill and the relative position of the void on the failure mechanism of the embankment. Lai [23] proposed a failure model for a reinforced embankment overlying a void with a full load on the embankment surface. For rigid pavements, this treatment is feasible.

In the case of flexible pavements, the vehicle traffic load is equivalent to a local overload acting on the embankment under road operational conditions. The effects of void depth, reinforced body stiffness and reinforced body burial depth on the bearing capacity of embankments under strip loading have been studied [24,25], but the failure mode of reinforced embankments overlying voids under local overload has not yet been investigated. The discrete element simulation technique based on the mechanics of particles can consider the discrete characteristics of soil particles, which can effectively reveal the failure mode and microscopic mechanism of soil structure [26,27].

In this paper, we take the reinforced embankment overlying voids under local overload as the research object, and establish a discrete element model based on a model test. We analyze the influence of void location on the bearing capacity characteristics of reinforced embankment, soil displacement field, contact force chain and the deformation law of the reinforced body, and reveal the failure mode of reinforced embankment overlying voids from a microscopic perspective.

## 2. Model Building

### 2.1. Test Profiles

Figure 1 shows a schematic diagram of the test model with dimensions of 600 mm × 300 mm. The width of the top surface of the embankment is 240 mm, the slope ratio of the embankment slope is 1:1.5 and the length of the geogrid is 255 mm (solid red line). The width of the embankment simulated in the test was 9.6 m and the height of the embankment was 0.8 m. Considering that the embankment is an axisymmetric structure, 1/2 of the embankment was taken for the test. The geometric ratio of 1:20 is used to reduce the size of the embankment and the glass fiber geogrid. Due to conditions, this test was not scaled down strictly based on similarity ratios, but the reinforced embankment overlying voids test is still of some research value.

In order to better represent the relative position of the void in the embankment, the vertical and horizontal positions of the void are expressed by H and L in the diagram, respectively, where the vertical distance H represents the distance from the top of the void to the bottom of the loading plate, and the horizontal distance L represents the distance from the core of the void to the center of the loading plate. The width of the loading plate B is 60 mm, the distance from the center of the loading plate to the wall at the edge of the model box is 120 mm, and the depth of the reinforcement body h is 30 mm.

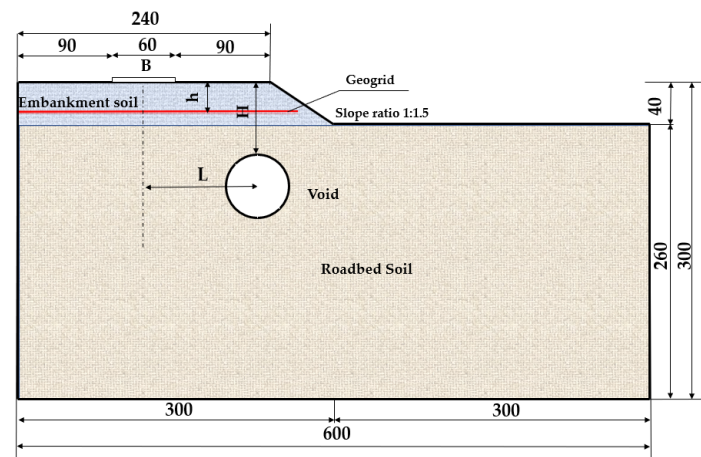


**Figure 1.** Test model (in mm).

The testing devices and materials mainly include the model box, loading and measuring devices, the geogrid and water pumping equipment (Figure 2). The size of the model box is 600 mm × 400 mm × 300 mm (length × width × height, respectively), and the dynamic and static triaxial loading device developed by the company GCTS, U.S.A., is used to load the soil body (the starting load is 0 kPa, and the loading speed is 3 N/s), which can achieve the real-time collection of load and top displacement data. The size of the loading plate is 288 mm × 60 mm × 30 mm (length × width × height, respectively), and the material of the loading plate is high-strength and low-density epoxy resin. The dynamic and static triaxial loading device is loaded in the center area of the loading plate, and geogrids are made of glass fiber material. The breaking strength of geogrids in the transverse and longitudinal directions is 60 kN/m, and the elongation at the break of the geogrid in the longitudinal and transverse directions is 6%. In addition, a soft plastic hollow cylinder with a diameter of 60 mm is used to simulate the void. A plastic membrane is wrapped around the inner and outer sides of the soft plastic cylinder, so that on the one hand, water is pumped inside the inner membrane by means of water pumping equipment to form a void, and on the other hand, the outer film prevents water from leaking into the soil.



(a)



(b)

**Figure 2.** Cont.

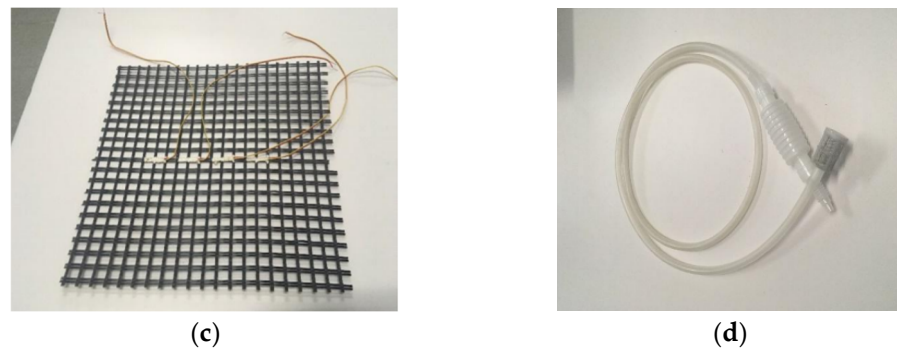


**Figure 2.** Schematic diagram of testing devices and materials: (a) model box; (b) loading and measuring devices; (c) geogrid; (d) water pumping equipment.

This laboratory test uses Fujian standard sand as a filler. After the sieve ratio test, it is determined that the particle size of the soil is mainly concentrated on the range of 0.5 to 2 mm. The gradation curve is shown in Figure 3 below, and the physical properties of the sand soil are shown in Table 1.

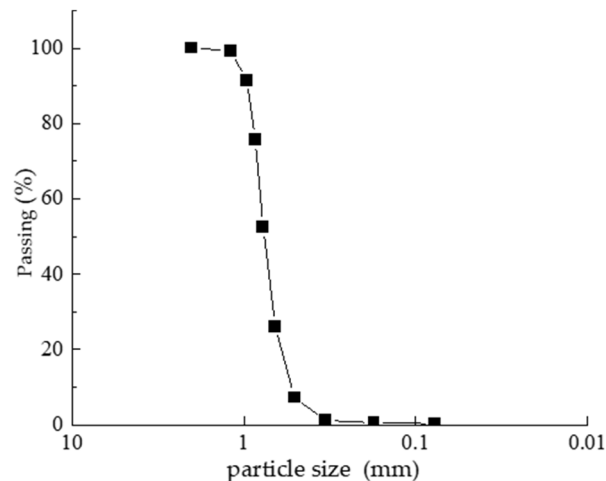


**Figure 3.** Grain size distribution curves of sandy soils.

**Table 1.** Physical properties of sandy soils.

| Property                                     | Value |
|--|-------|
| Gravity, $\gamma$ ( $\text{kN}/\text{m}^3$ ) | 17.03 |
| Specific gravity of particles, $G_s$         | 2.65  |
| Porosity ratio, $e$                          | 0.585 |
| Water content, $w$ (%)                       | 0.15  |
| Uniformity factor, $C_u$                     | 1.39  |
| Coefficient of curvature, $C_c$              | 0.94  |

## 2.2. Construction of Discrete Element Model

The PFC particle flow method decomposes the bulk system into discrete units, which are used as the basic units to visually express the interaction states and motion properties between the units at each moment in time. The software replaces the selection of the constitutive model of the material itself by setting the contact between particles. Since the discrete elements do not need to satisfy the deformation coordination relationship, it has a greater advantage in simulating the large deformation of discontinuous media such as soil. At present, the PFC software has become a recognized numerical simulation software and has penetrated into almost all directions in the field of geotechnical engineering.

Based on the above laboratory experiment dimensions, PFC2D software was used to establish a computational model of the reinforced embankment overlying a void, by generating spherical particles to simulate the sandy soil and the geogrid, and by creating wall units to simulate the model boxes and loading plates. Figure 4 shows a schematic of the numerical simulation model. In the model, blue particles represent soil particles, red particles represent the geogrid and blue lines represent walls. The surrounding boundary walls is fixed. The wall is a rigid body and does not produce deformation. The bottom surface of the loading plate is set as the horizontal observation surface M. The position of the observation surface M decreases as the loading plate decreases. The load  $P$  in the load–settlement curve is obtained by dividing the loading plate contact force  $F$  monitored on profile M by the loading plate width  $B$ . The settlement ratio  $S/B$  is obtained by dividing the wall displacement  $S$  directly monitored by the loading plate width  $B$  in the Fish language that comes with the PFC.

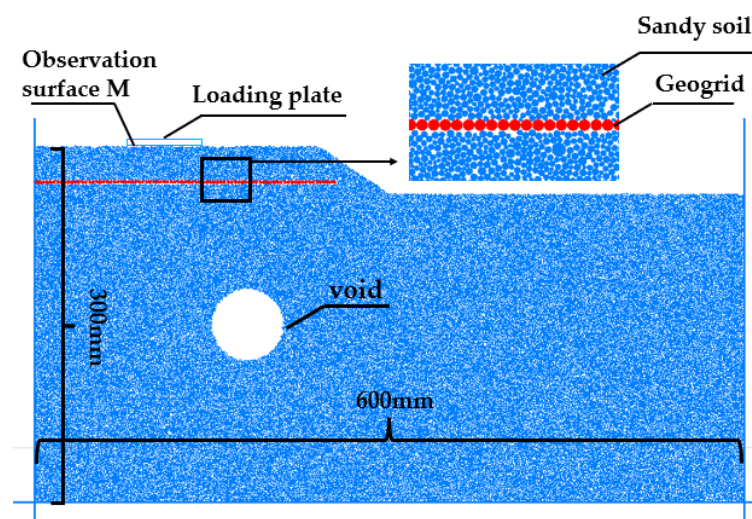


Figure 4. Numerical simulation model.

Based on the computational resources of the hardware, the generation of particles in discrete element software according to laboratory-tested soil particle grading curves is difficult to realize; therefore, it is necessary to extend the radius of the soil particles. When the radius multiplier is too small, the number of soil particles will be extensive while improving the accuracy of the simulation, and thus, the calculation cannot be converged; when the radius multiplier is too large, the simulation results of the discrete element will have a large deviation from the actual situation. Based on the requirements of calculation efficiency and simulation accuracy, this paper has made several attempts to enlarge the particle size of the soil, so as to obtain reasonable enlargement results. After attempts, we finally obtained a radius multiplier of 2, and the particle size of sandy soils in the simulation ranged from 1 to 4 mm. The porosity of the sandy soil was 0.17 upon converting from 3D to 2D [28]. The contact model of sandy soil was chosen as a linear contact model, the contact between particles of the geogrid was the parallel bonding model and the contact between sandy soil and geogrid was the linear contact model. The particle size of the geogrid was 1.5 mm. Based on the idea of inverse simulation, this paper has changed the microscopic parameters of the model to carry out a large number of simulations on sandy embankment, reinforced body tensile test and reinforced embankment load test, respectively, and compared the simulation results with the laboratory test results through the trial-and-error method, so as to finally obtain more reasonable microscopic parameters of the discrete element model. The microscopic parameters of each part of the material for the numerical simulation are shown in Table 2.

**Table 2.** Microscopic parameters of each material for the PFC model.

| Parameters  | Soils             | Geogrid              | Model Box            |
|---|-------------------|----------------------|----------------------|
| Normal contact stiffness of particles (N/m)         | $5.0 \times 10^8$ | $5.0 \times 10^9$    | $1.0 \times 10^{11}$ |
| Shear contact stiffness of particles (N/m)          | $5.0 \times 10^8$ | $5.0 \times 10^9$    | $1.0 \times 10^{11}$ |
| Normal stiffness of cementation (N/m <sup>3</sup> ) | —                 | $6.5 \times 10^8$    | —                    |
| Shear stiffness of cementation (N/m <sup>3</sup> )  | —                 | $6.5 \times 10^8$    | —                    |
| Normal strength of cementation (N/m <sup>2</sup> )  | —                 | $1.0 \times 10^{11}$ | —                    |
| Shear strength of cementation (N/m <sup>2</sup> )   | —                 | $1.0 \times 10^{11}$ | —                    |
| Friction coefficient                                | 0.8               | 0.6                  | 0.2                  |

Based on the microscopic parameters in Table 2, sandy embankments, reinforced bodies and reinforced embankments were built, and the discrete element simulation results were compared to the laboratory tests by changing the location of the voids. In order to better verify the accuracy of the model parameters, the following working conditions were established to compare the simulation and test results, respectively, to finally verify the rationality of the parameters; the specific working conditions are shown in Table 3.

**Table 3.** Comparison conditions.

| Work Conditions | Void Diameter (mm) | Reinforced Layers | H/B | L/B |
|-----------------|--------------------|-------------------|-----|-----|
| ZX1             | 0                  | 0                 | —   | —   |
| ZX2             | 60                 | 0                 | 2   | 0   |
| ZX3             | 60                 | 1                 | 2   | 0   |
| ZX4             | 60                 | 1                 | 2   | 1   |

Figure 5 shows the load–settlement curves of the embankment under the test and simulation, and Figure 6 is the stress–strain relationship curve for the uniaxial tensile test of the geogrid. From Figure 5, it can be seen that there is a certain gap between the discrete element test and simulated load–settlement curves, but the general trend is consistent, and the similarity between the two is high, and the peak bearing capacity remains at the same level. Therefore, it can be concluded that the sandy embankment and the reinforced embankment can be better simulated using the microscopic parameters in Table 2.

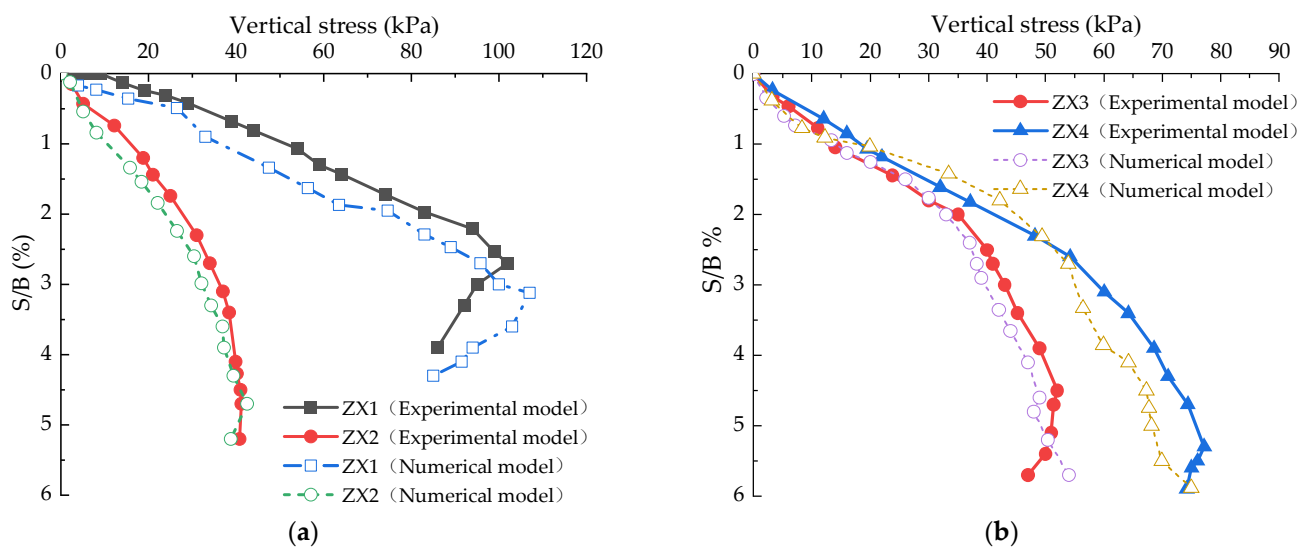


**Figure 5.** Load–settlement curve for the embankment: (a) sandy embankments; (b) reinforced embankments.

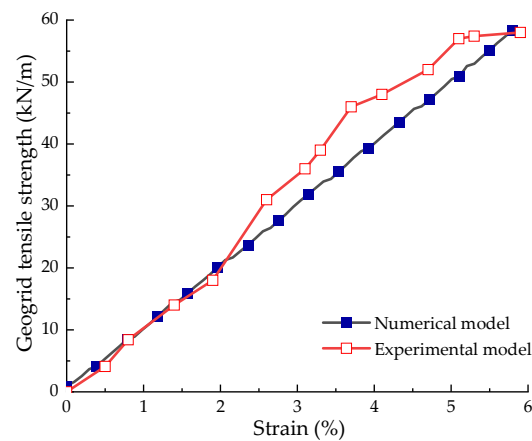


**Figure 6.** Geogrid stress–strain curve.

It can be seen from Figure 6 that there is a gap between the discrete element test and the simulated uniaxial tensile curves after loading for a certain period of time, which is due to the fact that the tensile strength of the reinforcing body in the indoor test changes with the increase in the strain of the reinforcing body, which is not taken into account in the discrete element simulation, but the general trend between the two is consistent. In both laboratory tests and simulations, the geogrid achieved a tensile strength of 60 kN/m at a strain of 6%. Therefore, the above selection of microparameters for the geogrid is reasonable.

This paper mainly analyzed the effects of different void locations on reinforced embankments under local overload conditions. To provide some basis for the design of reinforced bodies in the embankments overlying voids in practical engineering, the effects of vertical distance  $H$  or horizontal distance  $L$  on reinforced embankments overlying voids were analyzed, and the failure modes of embankment was proposed. The same loading speed was used for the models of different working conditions, and the specific simulation test scheme is shown in Table 4. The failure criteria in this paper are based on the provisions of the Engineering Geology Manual for foundation failure under shallow plate tests [29].

**Table 4.** Simulated operating conditions.

| Work Conditions | H/B | L/B |
|-----------------|-----|-----|
| A1              | 1   | 0   |
| A2              | 2   | 0   |
| A3              | 3   | 0   |
| B2              | 2   | 1   |
| C2              | 2   | 2   |
| D2              | 2   | 3   |
| E2              | 2   | 4   |

### 3. Results

#### 3.1. Characterization of Load Bearing Capacity

Figure 7 shows the embankment load–settlement curves at different void locations. Figure 7a shows the load–settlement curves at different  $H/B$ . The load–settlement curves of each working condition basically overlap under the first 5 kPa load case. After 5 kPa, load differences start to appear. When  $H$  increases from  $B$  to  $3B$ , the bearing capacity increases with the increase in the vertical distance  $H$  under the same foundation settlement. A3 and A2 have an increase of 2.5 times and 1.5 times, respectively, in the ultimate bearing capacity compared to A1. It can be seen from the above that the ultimate bearing capacity of the embankment increases non-linearly with the increase in  $H$ .

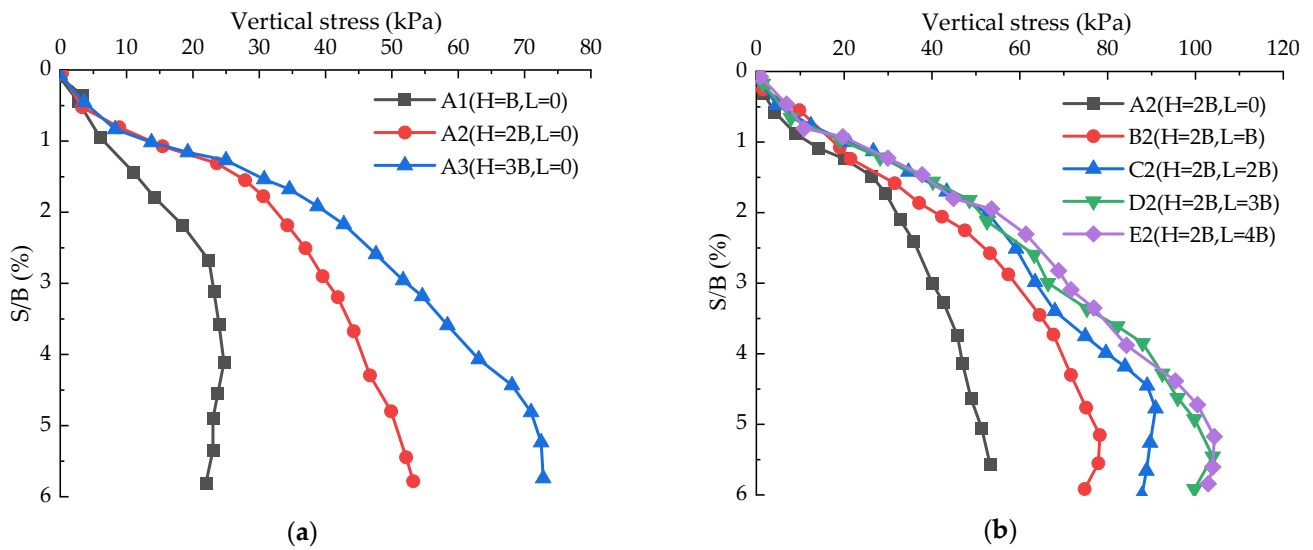


Figure 7. Load–settlement curves for different void locations: (a) at different H/B; (b) at different L/B.

From Figure 7b, it can be obtained that before the first 20 kPa load, the settlement curves of each working condition basically overlap, after 20 kPa load, there is a difference. When the horizontal distance L changes from 0 to 3B, the ultimate bearing capacity of the embankment increases with the increase in L. When  $L \geq 3B$ , the load–settlement curves of D2 and E2 basically coincide, the change in L has a small effect on the ultimate bearing capacity of the embankment at this point.

### 3.2. Analysis of Displacement Field

In order to analyze the effect of H/B on embankment soil displacement, three representative regions, 1, 2 and 3, were intercepted in the embankment. Region 1 and 3 are at the lower soil of the reinforced body, region 3 is further away from the loading plate compared to region 1, and region 2 is at the upper part of the reinforced body further away from the loading plate. Figure 8 shows a diagram of the relative positions of the regions (the solid red line represents the reinforced body).

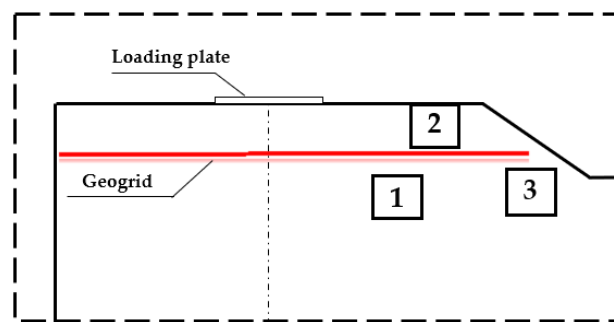
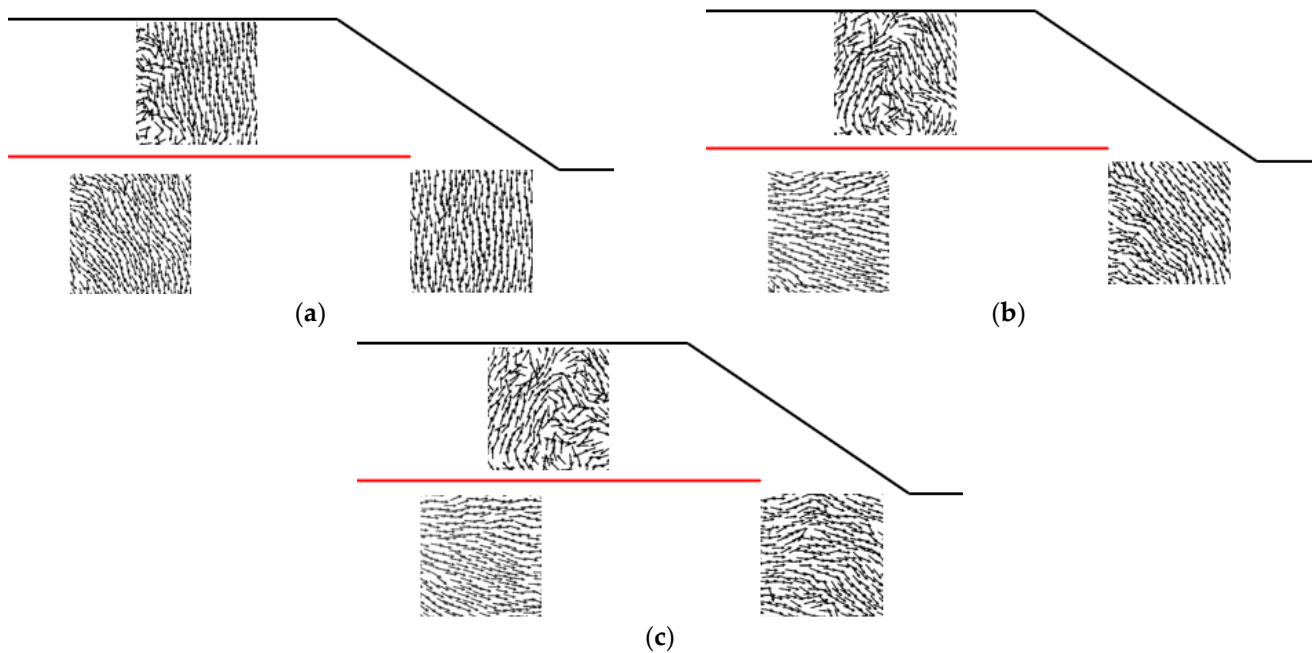


Figure 8. Schematic diagram of the relative positions of the regions.

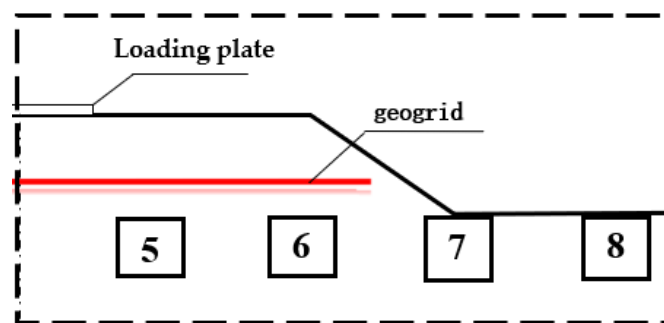
Figure 9 shows the displacement vector diagram of the soil inside each region of the embankment at different H/B. From the diagram, it can be obtained that when  $H = B$  (Figure 9a), the soil displacements in regions 1 and 3 are generally in a downward direction. The left part of region 2 is in a disorderly state, and other parts of region 2 is moving downward as a whole because of gravity. When  $H = 2B$  (Figure 9b), soil displacements are generally to the right in region 1 and generally downward in region 3. When  $H = 3B$  (Figure 9c), soil displacements are generally to the right in regions 1 and 3. As H/B increases, the soil in regions 1 and 3 is transformed from an overall downward vertical displacement to a horizontal displacement to the right. This is because as H/B increases,

the soils in regions 1 and 3 are subjected to more loads transferred from the embankment surface. The transferred loads cause a tendency for the displacements to move horizontally to the right. Comparing the soil displacement of region 2 at different  $H/B$ , it can be found that when  $H/B$  is transformed from 1 to 2, there is a significant increase in the width of the local slip surface in the upper part of the reinforced body, and when  $H/B$  is transformed from 2 to 3, the increase in the width of the slip surface is not significant at this time.



**Figure 9.** Soil displacement vector diagram of embankment at different  $H/B$ : (a)  $H = B, L = 0$ ; (b)  $H = 2B, L = 0$ ; (c)  $H = 3B, L = 0$ .

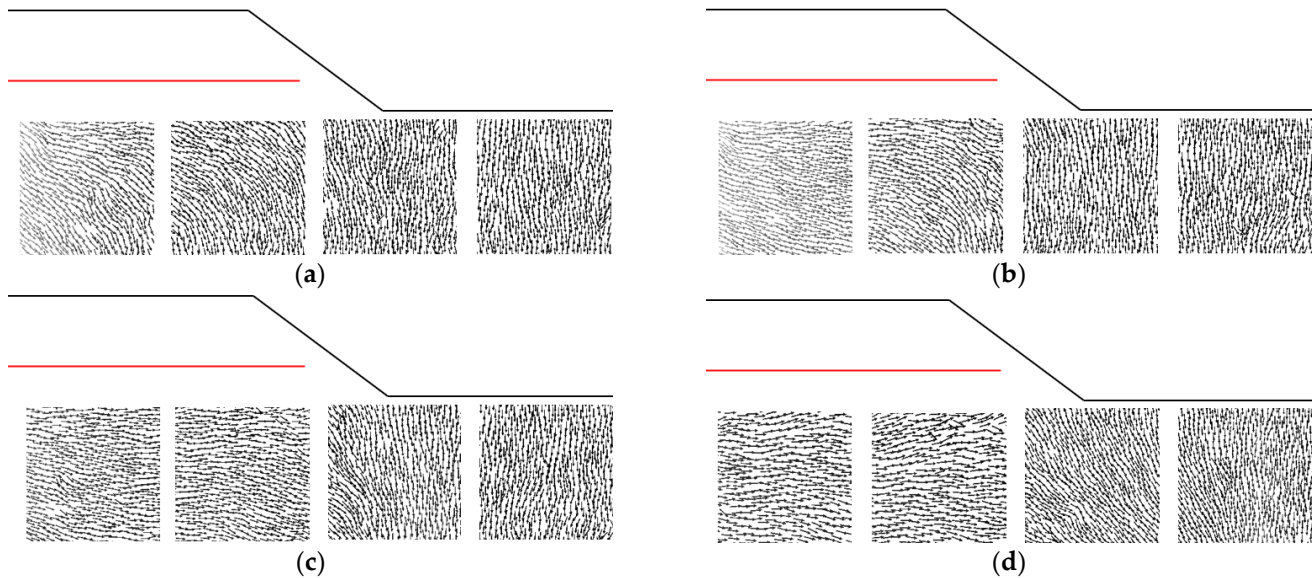
In order to analyze the effect of  $L/B$  on embankment soil displacement, the four regions, 5, 6, 7 and 8, were intercepted in the embankment. The depth of the four regions was the same, and the top of the region was equal to the road base surface. The distance between the center of each region and the center of the loading plate was  $B, 2B, 3B$  and  $4B$ , respectively. Figure 10 shows a schematic diagram of the relative positions of the regions (the solid red line represents the reinforced body).



**Figure 10.** Schematic diagram of the relative positions of the regions.

Figure 11 shows the soil displacement vectors in each region of the embankment at different  $L/B$ . When  $L/B$  is 1, 2, 3 and 4, respectively, the void is located directly below regions 5, 6, 7 and 8. When comparing the different  $L/B$  conditions, it can be found that the width of the soil region dominated by horizontal displacements in the upper part of the void gradually increases as  $L$  increases. When  $L/B < 4$ , the soil on the upper left side of the void is displaced horizontally to the right, while the soil on the upper part of the void and

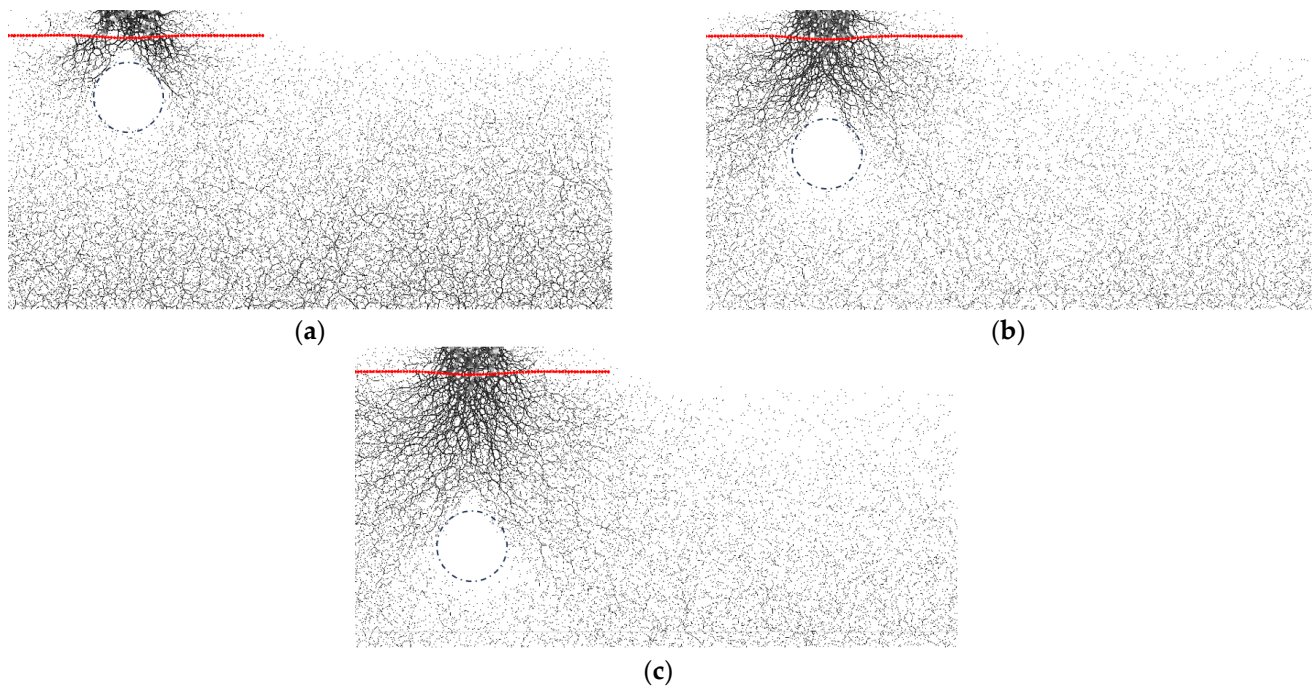
the upper right side of the void is moved downward. This is due to the fact that the load transmitted from the embankment surface acts on the upper left area of the void, which is much greater than the self-weight of the soil, which causes the soil to have a tendency to move horizontally to the right. When  $L$  changes, the soil displacement in region 8 is always predominantly downward, which indicates that the change in  $L$  has less of an impact on the soil in region 8.



**Figure 11.** Soil displacement vectors of embankment at different  $L/B$ : (a)  $H = 2B$ ,  $L = B$ ; (b)  $H = 2B$ ,  $L = 2B$ ; (c)  $H = 2B$ ,  $L = 3B$ ; (d)  $H = 2B$ ,  $L = 4B$ .

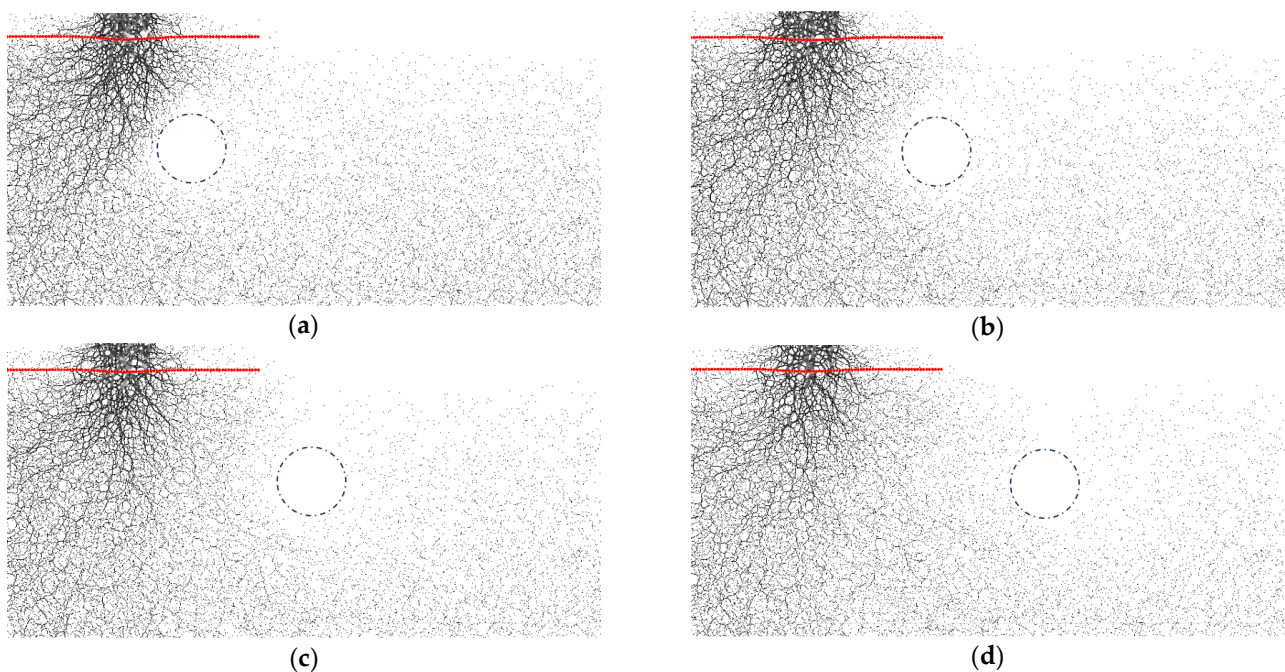
### 3.3. Analysis of Contact Force Chain

Figure 12 shows the contact force chain diagram of the embankment at different  $H/B$ , where the circular dashed line represents the position of the void and the red continuous particles represent the position of the reinforcement body. From the diagram, it can be seen that the contact force chain is columnar in the upper part of the reinforced body, and the contact force chain has a triangular blank area at the position above the void. The contact force chain extends from the embankment surface to both sides of the void. The contact force chain in the area below the void is thinner than in other areas at the same depth, due to the void preventing the transfer of load to the lower area of the void. When  $H/B = 1$  (Figure 12a), the void is close to collapsing into the lower part of the reinforced body, and the contact force chain at the bottom of the embankment is thicker at this time, which is due to the fact that the embankment is subjected to a smaller load, making the original contact force of the embankment soil relatively larger. As the vertical distance  $H$  increases, the contact force chain at the top of the void becomes denser and the number of thick chains increases, the embankment soil can withstand more load at this time.



**Figure 12.** Diagram of the contact force chain at different  $H/B$ : (a)  $H = B$ ,  $L = 0$ ; (b)  $H = 2B$ ,  $L = 0$ ; (c)  $H = 3B$ ,  $L = 0$ .

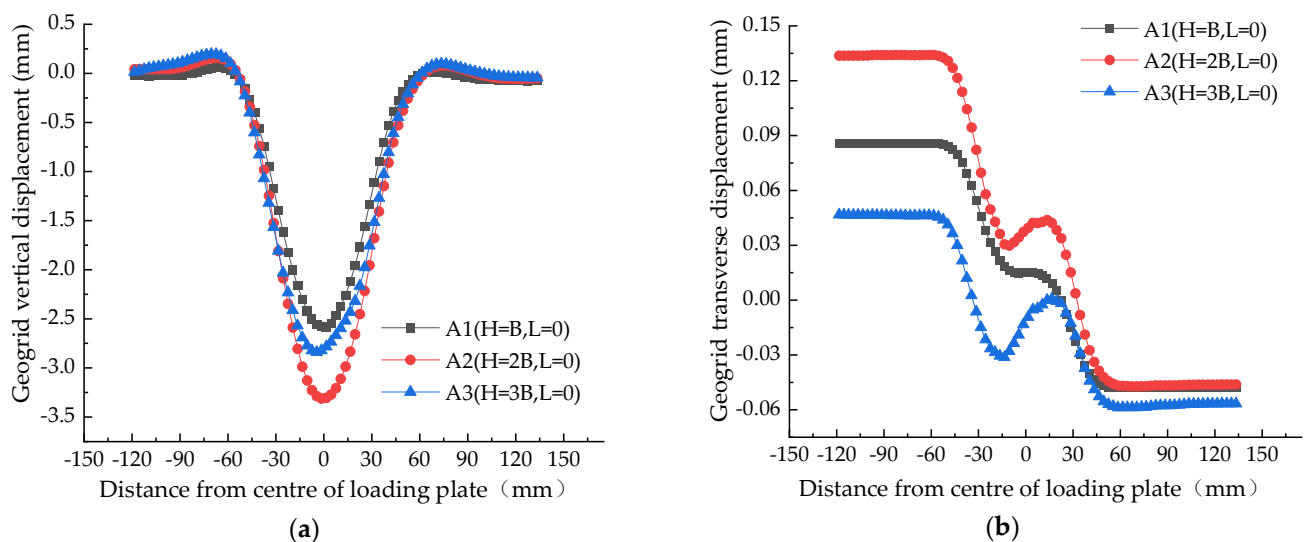
Figure 13 shows the contact force chain diagram of the embankment at different  $L/B$ . From the diagram, it can be obtained that the contact force chain on the left side of the void is significantly larger than that in the right side of the void in terms of coarseness and density of distribution, which indicates that the existence of the void prevents the transfer of the embankment surface load to the soil area on the right side of the void. By comparing the contact force chains at different  $L/B$ , it can be seen that the range of action of the coarse force chain gradually increases as  $L$  increases.



**Figure 13.** Diagram of the contact force chain at different  $L/B$ : (a)  $H = 2B$ ,  $L = B$ ; (b)  $H = 2B$ ,  $L = 2B$ ; (c)  $H = 2B$ ,  $L = 3B$ ; (d)  $H = 2B$ ,  $L = 4B$ .

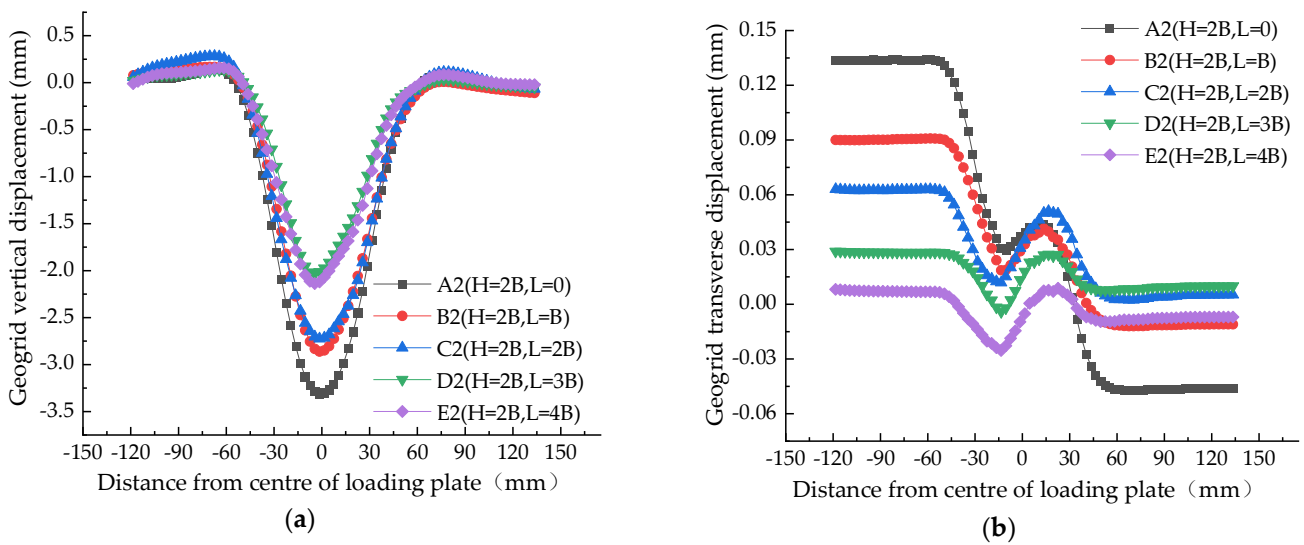
### 3.4. Deformation Analysis of Reinforced Bodies

Figure 14 shows the geogrid displacement curves of the embankment of different H/B at the time of failure. Figure 14a shows the vertical displacement curves of the geogrid at different H/B. From Figure 14a, the maximum vertical settlement of the geogrid shows a trend of increasing and then decreasing as H increases. The vertical displacement curve is symmetrical around the center of the loading plate, and the vertical displacement of the geogrid within a distance of 60 mm from the center of the loading plate is fitted with a quadratic parabola. The vertical displacement of the reinforced body gradually decreases with increasing distance from the center of the loading plate, and the vertical displacement approaches zero at 60 mm from the center of the loading plate. The deformation of the reinforcement body around 60 mm from the center of the loading plate shows a circular segment, and the geogrid in this area has a certain negative deformation, caused by the extrusion of the surrounding soil. Figure 14b shows the transverse displacement curves of the geogrid at different H/B. From the figure, the transverse displacement of the geogrid is centrosymmetric around the center of the loading plate (the direction of displacement of the geogrid is positive to the right), and the transverse displacement at the center of the loading plate increases and then decreases as H increases. The transverse displacement of the geogrid 60 mm outside the center of the loading plate remains almost constant; the transverse strain of the geogrid in this area is small.



**Figure 14.** Geogrid displacement curves at different H/B: (a) vertical displacement; (b) transverse displacement.

Figure 15 shows the geogrid displacement curves of the embankment at different L/B. From Figure 15a, when  $L \leq 3B$ , the maximum vertical displacement of the geogrid decreases as L increases, when  $L \geq 3B$ , the maximum vertical displacement of the geogrid roughly overlaps. The vertical displacement curves of the geogrid at different L/B are symmetrical around the center of the loading plate and decrease with increasing distance from the center. This indicates that the deformation of the geogrid under ultimate load is mainly influenced by the downward displacement of the loading plate and is less influenced by the horizontal distance L.



**Figure 15.** Geogrid displacement curves at different L/B: (a) vertical displacement; (b) transverse displacement.

From Figure 15b, it can be seen that the displacement direction of the geogrid at the center of the loading plate is to the right. The relative displacement of the reinforced soil interface on the left side of the geogrid is greater than that on the right side, probably due to the tendency of the soil at the lower right side of the geogrid to move toward the slope during the loading process, which drives the overall movement of the geogrid to the right. As L increases from 0 to 3B, the transverse strain rate of the geogrid at the edge of the loading plate (located 30mm from the center of the loading plate) decreases significantly. When L increases from 3B to 4B, the transverse strain rate of the geogrid at the edge of the loading plate does not change significantly, indicating that when  $L \geq 3B$ , the change of L has a low effect on the transverse strain of the geogrid.

### 3.5. Analysis of Failure Modes

When the embankment is broken, the stress direction of the soil around the void is not only affected by the relative displacement of the soil due to the void, but also by the upper load transmitted by the embankment surface, which leads to more complex deflection of the soil around the void. The main stress cross has obvious advantages in monitoring the stress deflection of the soil [30–32], and  $4 \times 4$  measurement circles are distributed in the area of  $80 \text{ mm} \times 80 \text{ mm}$  on the left and right side of the void, and  $10 \times 4$  measurement circles are distributed in the area of  $220 \text{ mm} \times 60 \text{ mm}$  in the upper part of the void. The radius of the measuring circle is 15 mm. Figure 16 shows the distribution of the measurement circles around the void.

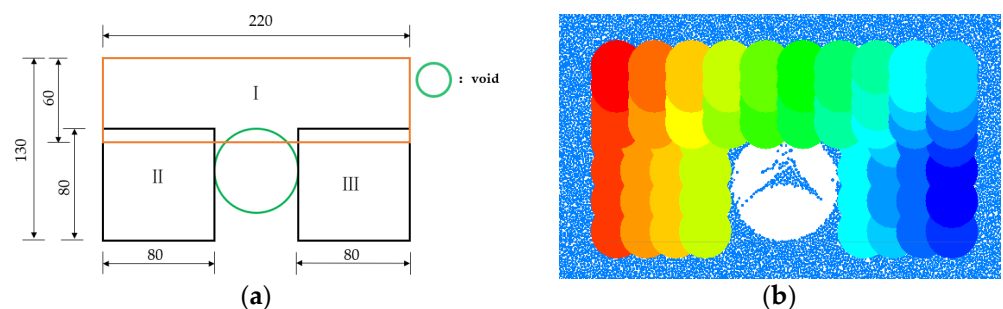


**Figure 16.** Schematic diagram of the measuring circle arrangement: (a) layout size chart; (b) measurement circle simulation diagram.

Taking  $L/B = 0$  as an example, the failure modes of embankment at different  $H/B$  are analyzed. Figure 17 shows the displacement vector field of the embankment during damage at different  $H/B$  and the stress deflection distribution around its void (red continuous solid line represents reinforced body; yellow border line represents the main stress measurement area). The length and direction of the line segments on the top right indicate the magnitude and direction of the principal stresses, with the long and short axes indicating the major and minor principal stresses, respectively.

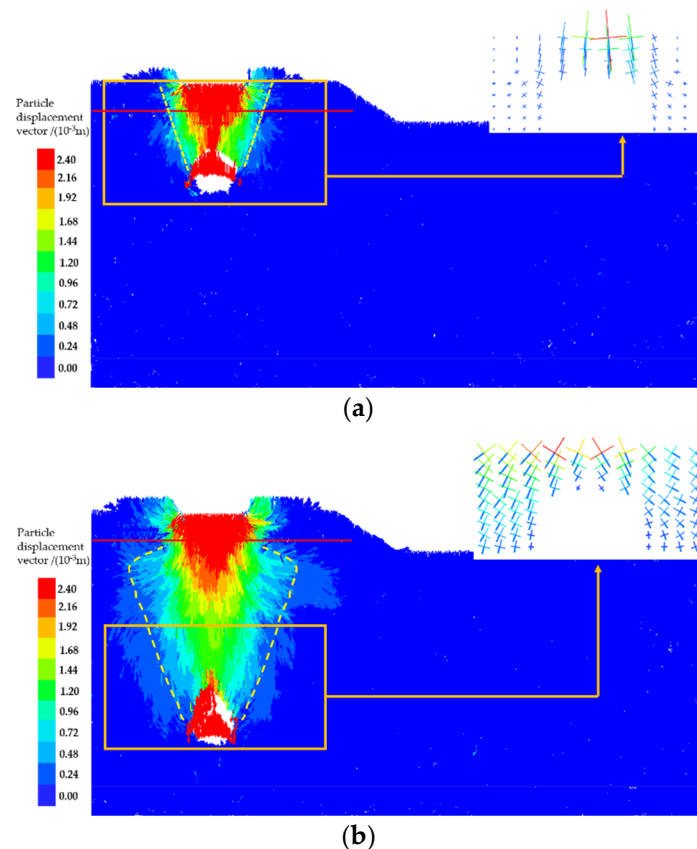


**Figure 17.** Displacement vector field and deflection of principal stresses around the void at different  $H/B$ : (a)  $H = B$ ,  $L = 0$ ; (b)  $H = 3B$ ,  $L = 0$ .

From the displacement vector diagram in Figure 17, we can see that when  $H = B$ , perforation failure occurs on the embankment, and the damage surface extends from the embankment surface to the side walls above the left and right of the void. The surface of the damage presents a basin type. The width at the top of the basin damage surface is greater than the width of the loading plate; this is because the loading plate's soil downward pressure under the plate has a horizontal extrusion effect. At this time, because the depth of the void is too small, the main stress direction above the void is mainly affected by the vertical load transmitted by the loading plate, and the main stress deflection is small. When  $H = 3B$ , a collapse perforation failure occurs on the embankment; the surface of damage still extends from the embankment surface to the side walls above the left and right of the void. It should be noted that at this time, the surface of damage in the lower side of the reinforced body as a whole is bottle-shaped, and the width of the damage surface in the reinforced body area has a significant narrowing. The main stress direction above the void produces a large deflection due to the relative displacement of the soil body, where there is a significant soil arching effect.

Taking  $H/B = 2$  as an example, the failure modes of embankment at different  $L/B$  are analyzed. Figure 18 shows the displacement vector field of the embankment during damage at different  $L/B$  and the stress deflection distribution around its void. From the

figure, the soil above the geogrid forms a local damage surface extending to the top of the embankment under the action of the embankment surface load. The presence of the geogrid prevents the surface of damage at the upper and lower interfaces of the reinforced soil from being connected, and the width of the damage surface is narrowed in the area of the geogrid.

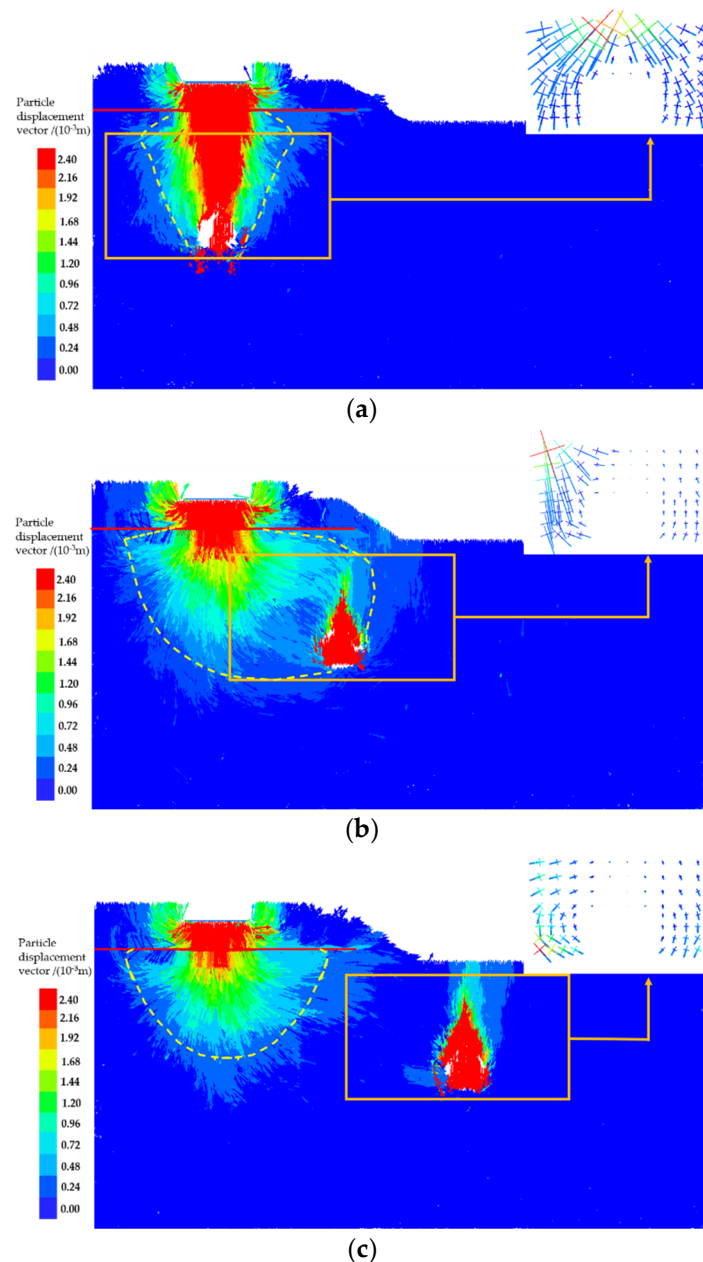


**Figure 18.** Displacement vector field and deflection of principal stresses around the void at different  $L/B$ : (a)  $H = 2B$ ,  $L = 0$ ; (b)  $H = 2B$ ,  $L = 2B$ ; (c)  $H = 2B$ ,  $L = 4B$ .

As shown in Figure 18a, when  $L = 0$ , at this time, the embankment is consistent with the failure mode in Figure 17b, i.e., when the collapse perforation failure occurs. The main stress of the soil around the void is deflected around the void, and the maximum stress area is concentrated in the upper part of the void. As shown in Figure 18b, when  $L = 2B$ , the damage surface extends from the embankment surface to the collapse area above the void and the lower left area of the void, forming a void side failure. At the same time, the void collapse causes less stress in the soil at the top of the void, and the transfer of embankment load makes the stress maximum area concentrated on the left side of the void, and the main

stress direction points to the void location. From Figure 18c, it is found that when  $L = 4B$ , the damage surface of the lower part of the geogrid presents a semi-circular arc, but does not extend to the void. At this time, the stress deflection around the void is mainly affected by the void, the main stress around the void deflects around the void and the soil arch effect is relatively obvious, forming a no impact failure.

#### 4. Conclusions

- (1) The ultimate bearing capacity of the embankment increases as  $H$  increases. When  $L < 3B$ , the ultimate bearing capacity of the embankment increases as  $L$  increases. When  $L \geq 3B$ , the change of  $L$  has less influence on the ultimate bearing capacity.
- (2) The existence of the void affects the embankment soil displacement. When  $0 < L \leq 3B$  and  $H = 2B$ , the soil on the upper left side of the void is displaced horizontally to the right, while the soil on the upper part of the void and the upper right side of the void is moved downward.
- (3) The void hinders the transfer of the load in the soil. When  $L = 0$ , the load is transferred to both sides of the void, and the contact force chain of the soil below the void is smaller. When  $L > 0$ , the load is mainly concentrated on the left side of the void, and the contact force chain on the left side of the void is obviously larger than that on the right side.
- (4) The maximum vertical deformation of the geogrid increases and then decreases with the increase in the vertical distance  $H$ . When  $L < 3B$ , the maximum vertical deformation of the geogrid decreases with the increase in the horizontal distance  $L$ , and when  $L \geq 3B$ , the change of  $L$  has less influence on the maximum vertical deformation of the geogrid. In summary, when the void is located directly below the loading plate, the deformation of the reinforced body is the largest. In the design of the reinforced body, it is safer to consider that the void is located directly below the loading plate.
- (5) When  $L = 0$ , as  $H$  increases, the failure mode of the embankment is transformed from perforation failure to collapse perforation failure, and when  $L > 0$ , as  $L$  increases, the failure mode of the embankment is transformed from void side failure to no impact failure.

**Author Contributions:** Writing—original draft preparation, Q.Z.; writing—review and editing, Y.L. All authors have read and agreed to the published version of the manuscript.

**Funding:** This research received no external funding.

**Institutional Review Board Statement:** Not applicable.

**Informed Consent Statement:** Not applicable.

**Data Availability Statement:** Data are contained within the article.

**Conflicts of Interest:** The authors declare no conflict of interest.

#### References

1. Villard, P.; Briançon, L. Design of geosynthetic reinforcements for platforms subjected to local. *Can. Geotech. J.* **2008**, *45*, 196–209. [[CrossRef](#)]
2. Giroud, J.; Bonaparte, R.; Beech, J.; Gross, B. Design of soil layer-geosynthetic systems overlying voids. *Geotext. Geomembr.* **1990**, *9*, 11–50. [[CrossRef](#)]
3. Blight, G.; Barrett, A. Field test of catenary net to protect traffic from mining subsidence. *J. Transp. Eng.* **1990**, *116*, 135–144. [[CrossRef](#)]
4. Briançon, L.; Villard, P. Design of geosynthetic-reinforced platforms spanning localized sinkholes. *Geotext. Geomembr.* **2008**, *26*, 416–428. [[CrossRef](#)]
5. Sireesh, S.; Sitharam, T.; Dash, S. Bearing capacity of circular footing on geocell-sand mattress overlying clay bed with void. *Geotext. Geomembr.* **2009**, *27*, 89–98. [[CrossRef](#)]
6. Yee, T.; Lawson, C. Serviceability limits for basal reinforced embankments spanning voids. *Geosci. Front.* **2011**, *2011*, 3276–3285.
7. Bridle, R.; Jenner, C. Polymer geogrids for bridging mining voids. *Geosynth. Int.* **1997**, *4*, 33–50. [[CrossRef](#)]

8. Flum, D.; Roduner, A.; Kalejta, J. Full-scale field tests for bridging sinkholes using flexible steel components as reinforcement. *Carbonates Evaporites* **2012**, *27*, 161–165. [[CrossRef](#)]
9. Kinney, T.; Connor, B. Geosynthetics supporting embankments over voids. *J. Cold Reg. Eng.* **1987**, *1*, 158–170. [[CrossRef](#)]
10. Huang, J.; Le, V.; Bin-Shafique, S.; Papagiannakis, A. Experimental and numerical study of geosynthetic reinforced soil over a channel. *Geotext. Geomembr.* **2015**, *43*, 382–392. [[CrossRef](#)]
11. Lu, W.; Zhang, Y.; Liu, W.; Liu, C.; Wang, H. Evaluation of geomembrane effect based on mobilized shear stress due to localized sinking. *Adv. Civ. Eng.* **2019**, *2019*, 4942578. [[CrossRef](#)]
12. Huckert, A.; Briançon, L.; Villard, P.; Garcin, P. Load transfer mechanisms in geotextile-reinforced embankments overlying voids: Experimental and analytical approaches. *Geotext. Geomembr.* **2016**, *44*, 442–456. [[CrossRef](#)]
13. Chevalier, B.; Villard, P.; Combe, G. Investigation of load-transfer mechanisms in geotechnical earth structures with thin fill platforms reinforced by rigid inclusions. *Int. J. Geomech.* **2011**, *11*, 239–250. [[CrossRef](#)]
14. Benmebarek, S.; Berrabah, F.; Benmebarek, N. Effect of geosynthetic reinforced embankment on locally weak zones by numerical approach. *Comput. Geotech.* **2015**, *65*, 115–125. [[CrossRef](#)]
15. Tran, V.; Meguid, M.; Chouinard, L. Three-dimensional analysis of geogrid-reinforced soil using a finite-discrete element framework. *Int. J. Geomech.* **2015**, *15*, 04014066. [[CrossRef](#)]
16. Le Hello, B.; Villard, P. Embankments reinforced by piles and geosynthetics-numerical and experimental studies dealing with the transfer of load on the soil embankment. *Eng. Geol.* **2009**, *106*, 78–91. [[CrossRef](#)]
17. Li, P.; Su, F. Unidirectional geosynthetic reinforcement design for bridging localized sinkholes in transport embankments. *Math. Probl. Eng.* **2022**, *2022*, 9577348. [[CrossRef](#)]
18. Feng, S.; Ai, S.; Chen, H. Membrane effect of geosynthetic reinforcement subjected to localized sinkholes. *Can. Geotech. J.* **2018**, *55*, 1334–1348. [[CrossRef](#)]
19. Chen, F.; Lin, Y.; Chen, S. Analytical solutions for geosynthetic-reinforced cohesive subgrade spanning trench voids. *Geotext. Geomembr.* **2020**, *48*, 854–866. [[CrossRef](#)]
20. Das, B.; Khing, K. Foundation on layered soil with geogrid reinforcement—Effect of a void. *Geotext. Geomembr.* **1994**, *13*, 545–553. [[CrossRef](#)]
21. Wu, G.; Zhao, M.; Zhao, H.; Xiao, Y. Effect of eccentric load on the undrained bearing capacity of strip footings above voids. *Int. J. Geomech.* **2020**, *20*, 04020078. [[CrossRef](#)]
22. Zhou, H.; Zheng, G.; He, X.; Xu, X.; Zhang, T.; Yang, X. Bearing capacity of strip footings on  $c-\phi$  soil with square voids. *Acta Geotech.* **2018**, *13*, 747–755. [[CrossRef](#)]
23. Lai, F.; Chen, F.; Li, D. Bearing capacity characteristics and failure modes of low geosynthetic-reinforced embankments overlying voids. *Int. J. Geomech.* **2018**, *18*, 04018085. [[CrossRef](#)]
24. Tahmasebipoor, A.; Noorzad, R.; Shooshpasha, E.; Barari, A. A parametric study of stability of geotextile-reinforced soil above an underground void. *Arab. J. Geosci.* **2012**, *5*, 449–456. [[CrossRef](#)]
25. Tafreshi, S.; Khalaj, O.; Halvaeae, M. Experimental study of a shallow strip footing on geogrid-reinforced sand bed above a void. *Geosynth. Int.* **2011**, *18*, 178–195. [[CrossRef](#)]
26. Fu, Z.; Chen, S.; Liu, S. Discrete element simulations of shallow plate-load tests. *Int. J. Geomech.* **2016**, *16*, 04015077. [[CrossRef](#)]
27. Zhang, J.; Liu, X.; Xiong, J.; Liang, L.; Zhang, W. Research on mechanical properties and failure mode of conglomerate based on discrete element method. *Appl. Sci.* **2023**, *13*, 223. [[CrossRef](#)]
28. Zhang, G. Researches on Meso-Scale Mechanism of Piping Failure by Means of Model Test and PFC Numerical Simulation. Ph.D. Thesis, Tongji University, Shanghai, China, 2007.
29. Editorial Board of Handbook of Engineering Geology. *Handbook of Engineering Geology*; Architecture and Architecture Press: Beijing, China, 2018.
30. Villard, P.; Huckert, A.; Briançon, L. Load transfer mechanisms in geotextile-reinforced embankments overlying voids: Numerical approach and design. *Geotext. Geomembr.* **2016**, *44*, 381–395. [[CrossRef](#)]
31. Rui, R.; Ye, Y.; Han, J.; Wan, Y.; Chen, C.; Zhang, L. Two-dimensional soil arching evolution in geosynthetic-reinforced pile-supported embankments over voids. *Geotext. Geomembr.* **2022**, *50*, 82–98. [[CrossRef](#)]
32. Anh Tran, Q.; Villard, P.; Dias, D. Discrete and Continuum Numerical Modeling of Soil Arching between Piles. *Int. J. Geomech.* **2019**, *19*, 04018195. [[CrossRef](#)]

**Disclaimer/Publisher’s Note:** The statements, opinions and data contained in all publications are solely those of the individual author(s) and contributor(s) and not of MDPI and/or the editor(s). MDPI and/or the editor(s) disclaim responsibility for any injury to people or property resulting from any ideas, methods, instructions or products referred to in the content.